ENGINEERING

Coherent spore dispersion via drop-leaf interaction

Zixuan Wu¹, Saikat Basu², Seungho Kim³, Mark Sorrells⁴, Francisco J. Beron-Vera⁵, Sunghwan Jung⁶*

The dispersion of plant pathogens, such as rust spores, is responsible for more than 20% of global crop yield loss annually. However, the release mechanism of pathogens from flexible plant surfaces into the canopy is not well understood. In this study, we investigated the interplay between leaf elasticity and rainfall, revealing how a flexible leaf structure can generate a lateral flow stream, with embedded coherent structures that enhance transport. We first modeled the linear coupling between drop momentum, leaf vibration, and the stream flux from leaf surfaces. With Lagrangian diagnostics, we further mapped out the nested coherent structures around the fluttering profile, providing a dynamical description for local spore delivery. We hope the mechanistic details extracted here can facilitate the construction of physically informed analytical models for local crop disease management.

Copyright © 2024 me 'Authors, some rights reserved; exclusive licensee American Association for the Advancement of Science. No claim to original U.S.
Government Works.
Distributed under a Creative Commons Attribution
NonCommercial
License 4.0 (CC BY-NC).

INTRODUCTION

Plant pathogens (i.e., viruses, bacteria, oomycetes, and fungi) have inflicted devastating damage to fourteen major crop species that support the bulk of food production every year (1–5). Specifically, biotrophic fungus species that cause commonly known rust diseases release microscopic airborne spores during the reproduction stage and execute the strategy of aerial long-distance dispersal for intercontinental range expansion across thousands of kilometers (5). This airborne nature of atmospheric transport is associated with hazards that traditional plant quarantine could not resolve (5). From a local pathogen management perspective, more work on how environmental factors, such as raindrops, influence spore liberation can benefit understanding and stopping dispersal at its origin (6).

Ambient wind and rainfall have been experimentally shown to facilitate the liberation of bioaerosols through the splashing and fragmentation of pathogen-bearing drops (1, 6-9). Local spore transport can be achieved by wet splashing of droplets with trapped particles below 100 µm (10). However, larger droplets (11) cannot sustain airborne transport from drift, thereby reducing their chances of escaping the plan canopy (10, 12, 13). Recent work has shown that dry dispersal away from the wheat leaf boundary layer is possible via raindrop-induced vortex flows (14). However, these experiments simulated impact conditions on a rigid and stationary substrate rather than a flexible one. Previous studies have shown that elastic energy stored in flexible plant or fungal structures is highly effective in ejecting bio-aerosols (15, 16). Literature has also documented that the flapping of flexible foils may generate intriguing flow structures regardless of wetting conditions (17-21). This shows an important aspect of spore dispersion that has not been studied: The triggered release of spores resulting from vibrations induced by droplets impacting flexible leaves, which may have low petiole flexural rigidity $(10^{-4} \text{ to } 10^{-5} \text{ N} \cdot \text{m}^2)$ (22).

In contrary to previous studies, our approach in this present work is to examine the issue of spore liberation focusing on the coupling between raindrop inertia, leaf elasticity, and flow generation. To achieve this, we develop an artificial system that simulates the interaction between raindrops, leaves, and particles. Through a combination of experimental and theoretical methods, we rationalize the formation of vortex stream flows along the edges of leaves in the two-dimensional (2D) transverse plane. To further unravel the coherent dispersion patterns and the escape routes, we use Lagrangian diagnostics commonly adopted in geophysical transport (23–25) to the vicinity of vibrating leaves. This analysis has enabled us to uncover the presence of the nested hyperbolic and elliptic Lagrangian coherent structures (LCSs) embedded within the vortex flow generated by raindrop impacts. By combining our predictive modeling and Lagrangian metrics, we aim to reveal here the full dynamical picture that can be triggered from raindrop-leaf interactions, which delivers particles as parcels on "fluid conveyor belts."

RESULTS

Experiments

Common wheat, *Triticum aestivum* (see Methods for preparation details), is used as a representative species as it is one of the most common crops susceptible to rust infection (14, 26). Wheat leaves used in this study have bending rigidity measured at $EI = 0.9 \pm 0.3 \times 10^{-5} \,\mathrm{Nm^2}$. Wheat leaf samples are measured at width, b = 10 to 20 mm, length, L = 150 to 200 mm, and thickness, th = 0.2 to 0.3 mm (see details of wheat leaf growth and preparations in section S1).

The drop impact experiment is conducted with a syringe pump (NE-1000, New Era Pump Systems) with deionized water droplet of radius $R_{\rm d}=1.2$ to 2.0 mm, released at different heights H=0.01 to 1.20 m onto a leaf/beam sample, as shown in Fig. 1A, resulting in impact velocity, $U_{\rm d}=0.4$ to 5.0 m/s. The choice of $R_{\rm d}$ and $U_{\rm d}$ yields

We = $\frac{\rho_d U_d^2(2R_d)}{\gamma}$ = 33 to 1400, which is a typical range for raindrop impacts (27–29). The longitudinal leaf axis is defined in \hat{x} , and the transverse leaf direction and vertical deflection are defined in \hat{y} and \hat{z} . The side view (xz plane) and top view (xy plane) of the wheat sample are shown in Fig. 1A. A uniform, thin layer (100 to 200 µm) of microparticles is deposited on substrate surface as spore surrogates, as shown in Fig. 1A, right inset.

A singular drop impact is released at 10 to 20 mm from the substrate tip to trigger the first-mode, free-end substrate vibration. Other impact conditions (multiple impacts, asymmetric, and off-tip impacts) initiate

¹Department of Mechanical and Aerospace Engineering, Cornell University, Ithaca, NY 14853, USA. ²Department of Mechanical Engineering, South Dakota State University, Brookings, SD 57007, USA. ³School of Mechanical Engineering, Pusan National University, Busan 46241, South Korea. ⁴School of Integrative Plant Science, Cornell University, Ithaca, NY 14853, USA. ⁵Department of Atmospheric Sciences, University of Miami, Miami, FL 33124, USA. ⁶Department of Biological and Environmental Engineering, Cornell University, Ithaca, NY 14853, USA.

^{*}Corresponding author. Email: sunnyjsh@cornell.edu

higher vibration modes and rotations that can be approximated as a super-position of the first-mode vibration and higher modes minor in magnitudes. Asymmetric impacts empirically shed smaller, daughter vortices minor to the primary generation. Therefore, the vortex dynamics in the first-mode vibration is the basis of dispersion that is focused here. Details of the variant impact conditions are characterized and summarized in section S2.

Energy of the system is injected via the impinging drop and then converted into airflow energy via the elastic potentials of the beam. For nondimensional analysis, Reynolds number of the drop is defined as ${\rm Re_d}=U_dR_d/\nu_d\approx 10^3$ to 10^4 , where ν_d is water kinematic viscosity taken as 8.9×10^{-7} m²/s. Reynolds number of the beam/leaf vibration is defined as ${\rm Re_b}=\overline{V}_bL/\nu_a\approx 10^2$ to 2.5×10^3 , where ν_a is the air kinematic viscosity as 1.5×10^{-5} m²/s. Here, the averaged beam speed is defined as $\overline{V}_b=2(\delta_{\rm max}-\delta_{\rm min})f$ for the first cycle, where $\delta_{\rm max}$ and $\delta_{\rm min}$ are the maximum and minimum deflection of the leaf substrate and f is the first-mode natural frequency of vibration. Particle Stokes number is defined as ${\rm St}=t_p/t_{\rm f},t_p=2/9\rho_p r_p^2/\mu_a$, is the particle relaxation time (Stokes time), where ρ_p,r_p , and μ_a are the particle density, radius, and the dynamics viscosity of air, respectively, $t_{\rm f}=\overline{R}_{\rm v}/\overline{V}_{\rm b}$ is the characteristic time of the carrying flow where the average vortex radius $\overline{R}_{\rm v}\approx A$ (vibration amplitude) and $\overline{V}_{\rm b}$ are chosen as characteristic length and velocity as the particles are dispersed via vortices.

Digital particle image velocimetry (DPIV) with smoke particles are used to extract the carrying fluid (air) velocity and vorticity fields, $\mathbf{u}(\mathbf{x},t)$ and $\boldsymbol{\omega}_{\mathbf{v}}(\mathbf{x},t)$. Particle tracking velocimetry with glass microparticles and pollen's is conducted to extract particle trajectories (see details in Methods and section S1).

Spore dispersion in impact-induced vibration

For spore liberation, spores are initially hygroscopically loosened up at the mature reproductive stage, allowing further release (30). During

drop impacts, surface vortices are generated and the spreading drop collides dynamically with the spores with forces (~10 nN) above the interparticle cohesion (~0.7 nN) (14), loosening spores further for dispersion. Vibration generates vortices at the two side edges and dislodges spores into surrounding vortices. The transport from leaf surface to vortices is discussed in detail in section S3, where three mechanisms are discussed: impact drop collision, impact vortex diffusion, and edge vortex attraction. The following analysis focuses on post-detachment delivery right after entrance into the ambient vortex flow.

Therefore, with these mechanisms above, initial impact and the first downstroke bring particles into the boundary layers and surrounding vortices at $\tau = \frac{t}{T} = 0$ to 0.25, with $\tau = 0$ defined at impact. Here, τ is dimensionless time normalized by the time period T = 1/f. At $\tau = 0.25$ to 0.50, sudden change in acceleration leads to the shedding of the impact vortex ring along with a stroke-reversal vortex of the opposite circulation as a dipole pair. Similar vortex dynamics in flapping is documented in the literature (20, 31, 32). The side view of such structure is visualized at $\tau = 0.5$ in Fig. 1B, with front view in Fig. 1C at $\tau = 0.5$. The shed vortex dipole can be seen in vorticity fields in Fig. 2E at $\tau = 3/8$. During the subsequent upstroke motion, $\tau = 0.50$ to 0.75, another upstroke vortex is generated and follows the leaf substrate upward until $\tau = 0.75$ at δ_{max} , the highest position of the substrate. This sequence is shown in Fig. 1 (B and C).

Immediately after the substrate reaches the peak, $\tau=0.75$ to 1.0, similar stroke reversal shedding dynamics is initiated to complete the cycle. The upstroke and downstroke vortices form a counter-rotating dipole during shedding as shown in Fig. 1 (B and C, right panels) confirmed by vorticity field in Fig. 2E at $\tau=7/8$. Preferential concentration of particles at certain regions is observed to develop, as particles are transported outward. This is shown in Fig. 1C at $\tau=0.8$ to 1.2, where particles form clustered structures as they expand outward in time. This is a clear indication of coherent flow development.

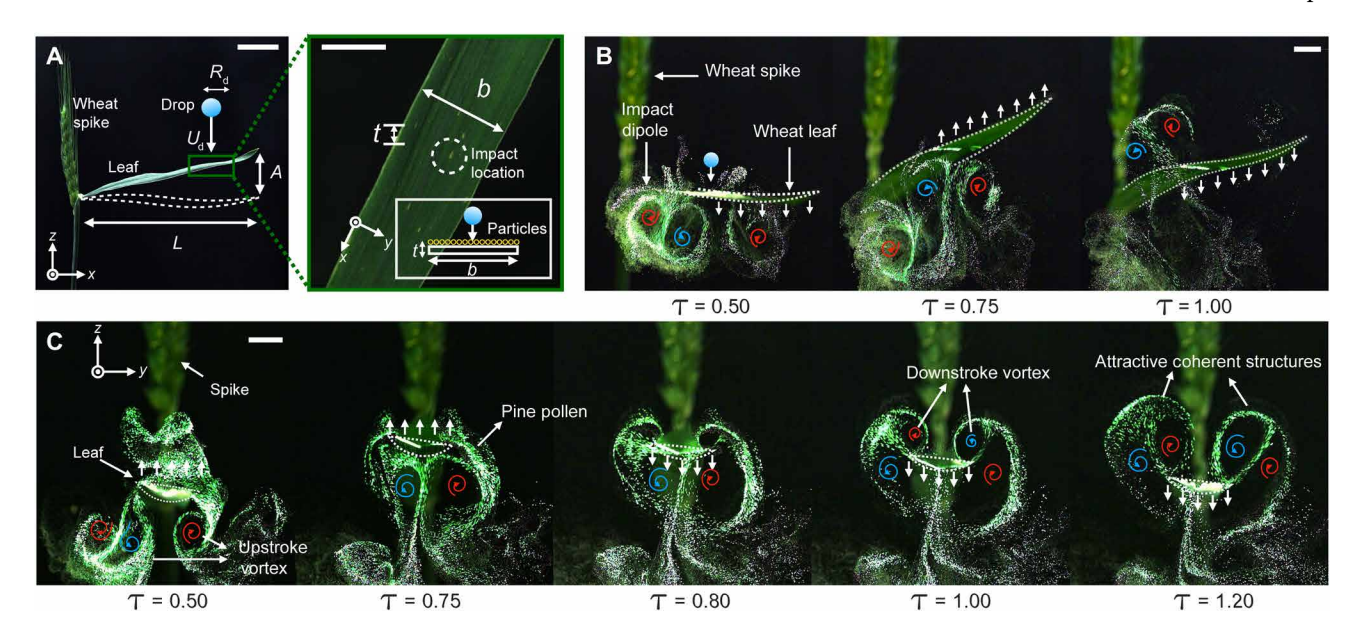


Fig. 1. Vortex-induced particle dispersal on wheat leaf surfaces. (A) Wheat leaf drop impact configurations in side view (left) and top view (right) and front view deposition schematics (inset). (B) Side view image sequences of wheat leaf impact experiments with particle deposited, from $\tau \in [0.5 \ 1.0]$ ($\tau = 0$ at impact). The drop momentum and size are $[U_d, R_d] = [3.13 \ m/s, 1.6 \ mm]$. Color coding indicates vorticity direction. (C) Front view image sequences of leaf-induced dispersion from $\tau \in [0.5 \ 1.2]$. Corresponding videos of (B) and (C) are in movie S1. Scale bars, 50 mm [(A), right] and 10 mm [(A) (left) and (B) and (C)].

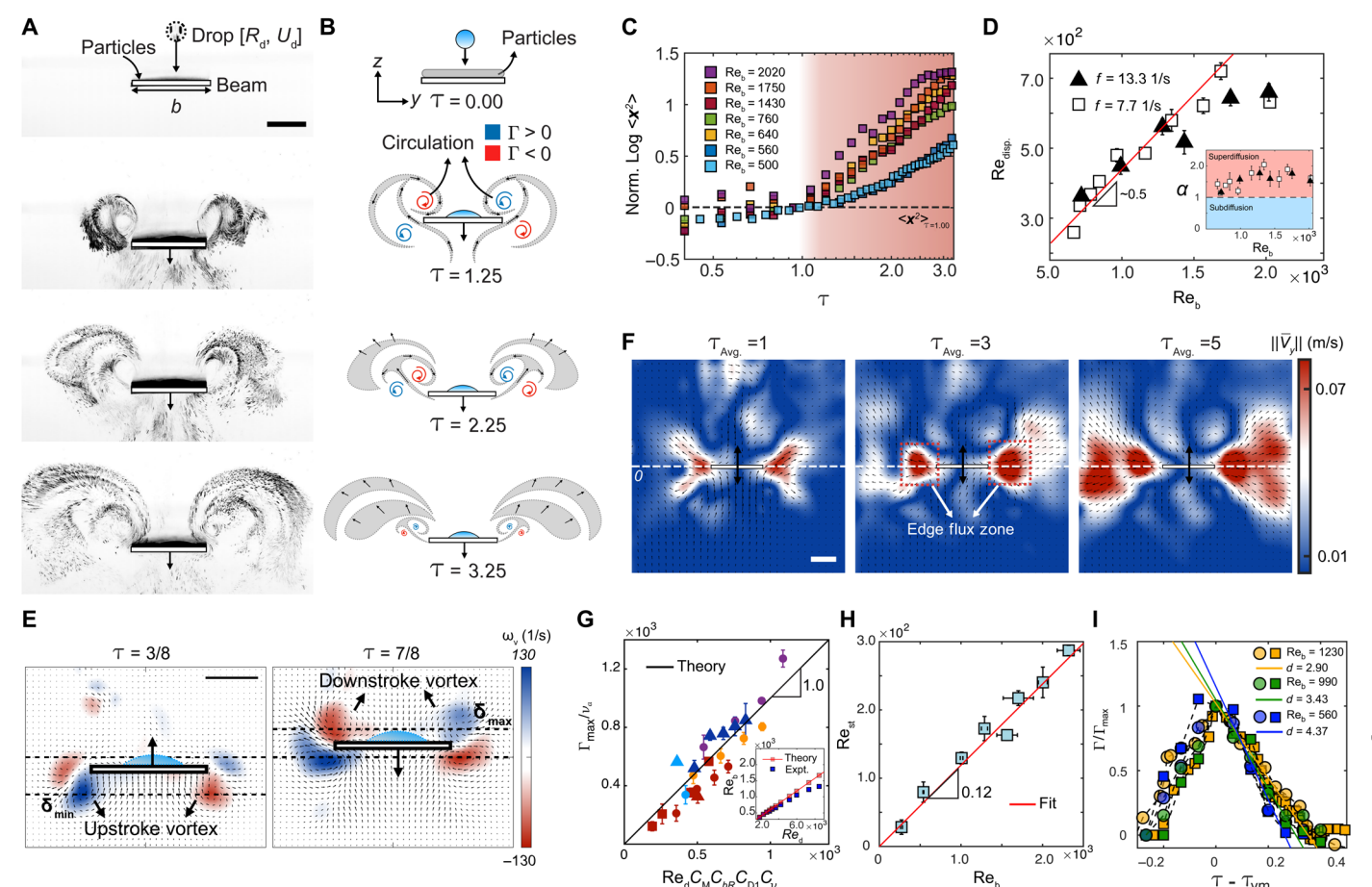


Fig. 2. Characterization of dispersion and flow generation. (**A**) Flow trace visualization of dispersion on surrogate beam from $\tau = 0.00$ to 3.25. Corresponding videos is in movie S2. Impact condition is $[U_d, R_d] = [1.72 \text{ m/s}, 1.60 \text{ mm}]$ on a L = 80 mm and b = 20 mm beam. (**B**) Corresponding schematics of dispersion steps in (A). (**C**) Normalized MSD of particles from the beam center over two cycles from $\tau = 0$ to 3.25 on log scale. It is normalized by shifting it vertically to align at $\tau = 1.00$ (beginning of enhanced dispersion). (**D**) Reynolds number of the particle dispersion across the range of Re_b. Inset provides the power α at different Re_b. (**E**) Vorticity field (ω_v) plot of the upstroke and downstroke vortices at $\tau = 3/8$ to 7/8. (**F**) Colormap of the average horizontal velocity field \overline{V}_y (in \hat{y} direction) over a period of $\tau = 1$ to 5. The velocity vector fields include the vertical direction velocity. Impact condition is $[U_d, R_d] = [2.80 \text{ m/s}, 1.60 \text{ mm}]$. (**G**) Normalized circulation versus Re_dC_MC_{DR}C_{D1}C_ν. Different symbols correspond to different drop-beam conditions (see Methods). Inset here shows Re_d versus Re_b in experiments and theory. (**H**) Reynolds number of the stream versus Re_b. (**I**) Normalized circulation (measured on left edge, normalized by the peak circulation) across time for different Re_b system. Time periods are aligned at the maximum circulation time τ_{vm} . Scale bars, 10 mm (for all panels).

To describe these coherent flows in the dynamics, we use the concept of LCS, a set of fluid parcels with attractive or repulsive properties for neighboring materials (23). The growth of these coherent profiles enhances mixing, divides up flow regions and ejects particles in specific pathways. The repetition of the described shedding cycle, enabled by leaf elasticity, produces an outward flow stream with nested layers of LCS, in which the particle cluster grows and expands under a defined dynamical sequence. Therefore, detailed LCS diagnostics is needed and used in later section to reveal the delivery pathways.

The wake patterns under the Reb tested are in a transition regime between 2S and 2P (33), depending on the vibration amplitude. We primarily focus on the low-amplitude 2S cases, while it should be noted that higher shedding modes exist. For the dominantly 2S scenarios, flow asymmetry is observed in the shedding stream about the leaf width axis, meaning vortex dipoles are shed "upward" relative to the width axis. Traditionally asymmetry is primarily induced by flow mechanics and beam geometry (34). However, we empirically observe that asymmetry is introduced by two factors here. First, gravity deflection on drop and beam causes asymmetric vibration profile

about the lateral y axis. Second, time separation of the peak vortex strength between the young downstroke vortex and the older, decaying upstroke vortex, biases the shedding angel at 45 above the width axis. This lifts the center shearing layer upward as shown in Fig. 1C at $\tau = 1.2$. Therefore, asymmetric shedding is observed here and in later LCS analysis.

In the following analysis, we first parametrically investigate the relationship among Re_d , Re_b , vorticity, and dispersion efficiency of the generated flow. A reduced-order free-end vibration model is built experimentally with thin polycarbonate cantilever beams to simulate the first-mode leaf vibration. Wheat leaves have high aspect ratios $C_{bL} = L/b = 2 - 8$, which makes the thin-beam surrogate model appropriate (see Discussion for how the current modeling extends to lower C_{bL} leaf systems, unlike wheat).

Vortex system and dispersion capacity

Using a beam surrogate model, dispersion stream flow from vibrating surface is visualized experimentally as shown in Fig. 2A (see corresponding video in movie S2). The corresponding schematics

illustrating the dispersion process are presented in Fig. 2B. These figures demonstrate the observed patterns of dipole shedding, which exhibit a bias towards the upper plane mentioned. To quantitatively analyze the dispersion, we calculated the mean square displacement (MSD) $\langle x^2 \rangle$ of the particle clusters at different Reb, as shown in Fig. 2C. The normalized MSD is defined as $\langle x^2 \rangle - \langle x^2 \rangle_{\tau=1.00}$. This highlights an enhanced dispersion period that can be observed in Fig. 2A. Further information regarding the extraction of MSD and non-normalized plots can be found in section S4.

The relation between Reb and the average particle dispersion speed $\overline{V}_{\rm disp.}$ (nondimensionalized as ${\rm Re_{disp.}} = \overline{V}_{\rm disp.} L/\nu_{\rm a}$), is also extracted and presented in Fig. 2D. We approximated the dispersion speed $\overline{V}_{\rm disp.}$ as $\overline{V}_{\rm disp.} \approx \langle x^2 \rangle / \tau$, the overall average dispersion rate. A positive correlation is observed for beams of different rigidity, with $Re_{disp.} \approx$ $Re_b/2$ for $Re_b < 1800$ in a linear approximation. Examining the relationship between MSD and time, $\langle x^2 \rangle \sim \tau^{\alpha}$, we found that the exponents α fall within the range of 1.0 to 2.0. This suggests a combination of diffusion and advection processes contributing to dispersion. Therefore, for the tested range of Re_b \approx 500 to 2000, the dispersion stream is consistently super-diffusive. Specifically, α increases at Re_b \approx 500 to 1400, indicating strengthening advection from beam vibration. The dispersion rate, however, does not increase at the same rate at Re_b > 1800, and α tends to decrease instead of reaching above 2.0 at Re_b = 1400 to 2000. Empirically, we attributed this to an observed turbulence increments in the flow, which disrupts the quasi-steady formation of lateral flow stream.

To understand the origin of this stream flow, average velocity fields over $\tau \in [1.0 \ 5.0]$ are extracted from DPIV, shown in Fig. 2F, indicating increasing outward $|\hat{y}|$ velocity, \overline{u}_{y} , in the field. A cone-shaped advection corridor is observed with the average flow field, proving the existence of a vibration-generated stream flow that expands outward. We also observed edge flux zone denoted by high outward velocity near the two edges. A mechanical model is thus constructed based on 2D beam potential and drop-beam kinematics to model the average velocity magnitude of the edge flux zones with drop inertia, beam conditions, and the generated vorticity.

We define here the complex coordinates on the yz plane as $\zeta = y + iz$, the complex velocity as $\chi = u_y - iu_z$ and the complex potential as Φ . By applying boundary condition $u_{z,\pm} = V_b(t)$ on the plate, where $V_b(t)$ and $u_{z,\pm}$ are vertical beam velocity and solution for u_z directly above and below the beam, respectively, solution of u_y , u_z on a thin

vibrating beam is obtained as
$$u_{y,\pm} = \pm V_b \frac{y}{\sqrt{\left[\left(\frac{b}{2}\right)^2 - y^2\right]}}; u_{z,\pm} = V_b$$
. By

calculating the circulation on the left edge vortex, we obtained $\Gamma_L = b \ V_b(t)$ (details of complex potential analysis is placed in section S4).

We then couple it with the drop-beam interactions, with $\delta(t) \sim (U_{\rm d}/f)e^{\varsigma \omega t}\sin(\omega t)$ (18), where ω and ς are the first-mode natural frequency and a damping coefficient, respectively. Evaluating at $\tau = 0.5$ (maximum circulation over the damped vibrations), we obtain

$$|\Gamma_{\text{max}}|/\nu_{\text{a}} = \text{Re}_{\text{d}}C_{\text{M}}C_{\text{bR}}C_{\text{D1}}C_{\nu} \tag{1}$$

Here, $C_{\rm M} = \frac{m_{\rm d}}{2m_{\rm d} + m_{\rm b}}$, where $m_{\rm d}$ and m_b are the drop and beam mass, respectively; $C_{bR} = b/R_{\rm d}$ is the width-drop-radius size ratio;

 $C_{\rm D1}=\pi e^{-\pi\varsigma}$, a constant with damping coefficient; and $C_{\nu}=\nu_{\rm d}/\nu_{\rm a}$, ratio of drop-air kinematic viscosity. The theoretical derivation is corroborated by experiments, as shown in Fig. 2G, in which circulations tested from different drop-beam conditions collapse onto the predictions. Reynolds number of the beam can be predicted as Re_b = Re_d $C_{\rm M}C_{LR}C_{\rm D2}C_{\nu}$, where $C_{LR}=L/R_{\rm d}$ and $C_{\rm D2}=e^{-(3\pi/2)\varsigma}+e^{-(\pi/2)\varsigma}$. The relation is confirmed from the inset of Fig. 2G. Therefore, we can also derive an average circulation strength over the first period as $\overline{\Gamma}=\frac{b\overline{V}_{\rm b}}{C_{\rm c}}={\rm Re_b}\frac{C_{LR}}{C_{\rm c}}$.

riod as $\frac{\overline{\Gamma}}{v_a} = \frac{b\overline{V}_b}{v_a} = \text{Re}_b \frac{C_{LR}}{C_{bl}}$.

The stream flow originates in the u_θ velocity component of the upstroke and downstroke vortices when they follow and shed off of the beam edge. These two counter-rotating vortices both provide an outward $|\hat{y}|$ flux on the beam edges, resulting as the edge flux zone (in red) in Fig. 2F. Therefore, to model the average stream flux speed on the edge, $V_{\rm st}$, we assume two separated Rankine vortices and integrate the time-average \hat{y} flux as the sum of time-average angular velocity \bar{u}_{θ} : $2\int \overline{u}_{\theta}dr = \frac{\overline{\Gamma}}{\pi}\int_{0}^{\overline{R}_{v}} \frac{r}{\overline{R}_{v}^{2}}dr = b\overline{V}_{b}/(2\pi)$, where \overline{R}_{v} is the average radius of the circulation (see schematic for the edge flux modeling in section S4). This \hat{y} edge flux is approximated experimentally by integrating the average \overline{V}_y vertically around the edge flux zone shown in Fig. 2F as $b\overline{V}_{\rm st} = \int_{-b/2}^{b/2} \overline{V}_y \, dl$. Integration line segment $z \in [-b/2 \, b/2]$ is chosen empirically as it covers the edge flux zone well for all cases. A ratio of the corresponding stream flux Reynolds number, $Re_{st} = V_{st}L/\nu_a$, to the beam Reynolds number becomes Re $_{\rm st}$ / Re $_{\rm b}=\overline{V}_{\rm st}/\overline{V}_{\rm b}=1$ / $(2\pi)\approx0.16.$ Experimentally, the slope is obtained as 0.12 (Fig. 2H), a decent agreement considering variability in vortex locations. The linear relationship is corroborated by previous studies on jet stream in the longitudinal direction (34).

Lastly, the shed vortices show a rapid decay that can be approximated linearly, following a relation of $\Gamma/\Gamma_{max} = -d(\tau - \tau_{vm})$, in which τ_{vm} is the time of peak circulation and d is a dimensionless decay rate (2.5 to 4.5) that decreases with increasing Re_b, as shown in Fig. 2I. This is reasonable as faster stream flux reduces vortex annihilation. The vortices are created and get dissipated quickly in $\tau < 0.5$. Therefore, particle dispersion is carried out by the stream flow generated via a defined dynamical process described by LCS in the next two sections and not by individual traveling vortices.

Spore expulsion by elliptic LCS

To investigate the dynamics of dispersion, particularly the downstroke leading to the enhanced dispersion period ($\tau = 0.75$ to 1.25), two types of LCS, elliptic and hyperbolic LCSs, are used. The carrying fluid of dispersion is air here; therefore, the LCS extracted and presented below is inertial in nature, commonly referred to as inertial LCS (iLCS). For simplification, we refer to them as LCS throughout. We used elliptic structures, or referred as rotationally coherent vorticies (35) below to objectively describe the vortex structure and its role in spore expulsion. For its diagnosis, Lagrangian averaged vorticity deviation (LAVD), an objective quantity defined by

$$LAVD_{t_0}^{t_0 + \tau_i T}(\mathbf{x}_0) = \int_{t_0}^{t_0 + \tau_i T} |\Omega[F_{t_0}^t(\mathbf{x}_0), t] - \overline{\Omega}(t)| dt$$
 (2)

is used. The method objectively identifies the vortices in the unsteady flow by finding the concentrated high-vorticity regions

from integration of t_0 to $t_0+\tau_i T$, with t_0 as the start of integration and τ_i as the dimensionless integration period. $\Omega[F_{\underline{t_0}}^t(\mathbf{x}_0),t]$ denotes the vorticity of the fluid over the flow map $F_{t_0}^t$, and $\overline{\Omega}$ is the vorticity at time t averaged over the tracked fluid bulk.

Empirically, $|\tau_i|=0.25$ to 0.50 is the integration time that captures the fluid structures in a cycle, as vortex dipole growth and shedding complete within a half cycle $\tau=0.5$. The resulting LAVD map is shown in Fig. 3B for the first downstroke $\tau=0.75$ to 1.25 (see movie S3). Boundaries of the coherent vortices are calculated and marked in Fig. 3B (black outlines). Start (τ_0) and end (τf) time of integration for the LCS structures are labeled on the plots and captions in Figs. 3 and 4.

To characterize the expulsion flux from such vortex, we define a flux criterion \mathscr{F} to describe the inertial particle ejections in Eq. 3 for the fluid regions within said boundary, labeled as $\mathcal{V}(t)$ (see full LAVD sequence and details of LAVD, flux calculations in section S5).

$$\mathcal{F} \propto t_p \frac{1 - R_{\rho}}{1 + R_{\rho}/2} \iint_{\mathcal{V}(t)} QdS \tag{3}$$

Q is the Okubo-Weiss criterion (36), defined here as $\omega_v^2 - S_s^2 - S_n^2$. ω_v is the relative vorticity, S_s is the shear strain, and S_n is the normal strain. Inside a Lagrangian vortex, Q > 0 (36). The flux calculation thus predicts a positive outward flux \mathscr{F} from vortex centers for inertial particles with density ratio $R_p = \rho_a/\rho_p \ll 1$, where ρ_a is the air density. Coherent vortex calculated from inertial particles here demonstrate strong expulsion behavior as the coherent vortex boundary expands

rapidly, shown in Fig. 4C for τ = 0.50 to 0.75. Therefore, the coherent vortices identified here effectively serve as traveling sources of outward spore flux near leaves.

Strength of flux increases in proportion to the particle response time and effectively the Stokes number $t_{\rm p} \propto$ St and the integral of Q. This flux relation is experimentally validated in Fig. 4D by the boundary expansion ratio of the coherent vortex, $R_{\rm exp} = S/S_0$, in which S_0 is the coherent vortex size before expansion and S is the expanded size at $\tau = 0.75$. Sample systems with higher Re_b and St, denoting stronger circulation and particle inertia, display the highest expansion on average as shown. The absolute sizes of the coherent vortex over time can be found in section S5.

Spore transport by hyperbolic LCS

Interactions of vortex structures during their growth and shedding organize the airflow near the leaf into nested hyperbolic LCS, which attract or repel particles readily ejected by the vortices.

To identify hyperbolic LCS, finite-time Lyapunov exponent (FTLE) diagnostics is initially applied, outputting the flow separation rate for the 2D yz domain (see calculation details in section S6). Briefly, the calculation takes a infinitesimal perturbation around a point $x(t_0)$, expressed as $|\delta x(t_0)|$, and extracts the exponent of the perturbation growth σ in real-time $\tau_i T$:

$$|\delta \mathbf{x}(t_0 + \tau_i T)| = e^{\sigma \tau_i T} |\delta \mathbf{x}(t_0)|$$
(4)

Observing the dynamics backward in time τ_i < 0, regions with the largest perturbation growth (high σ) reveal the most attractive surfaces as they pull together fluid elements furthest apart, namely,

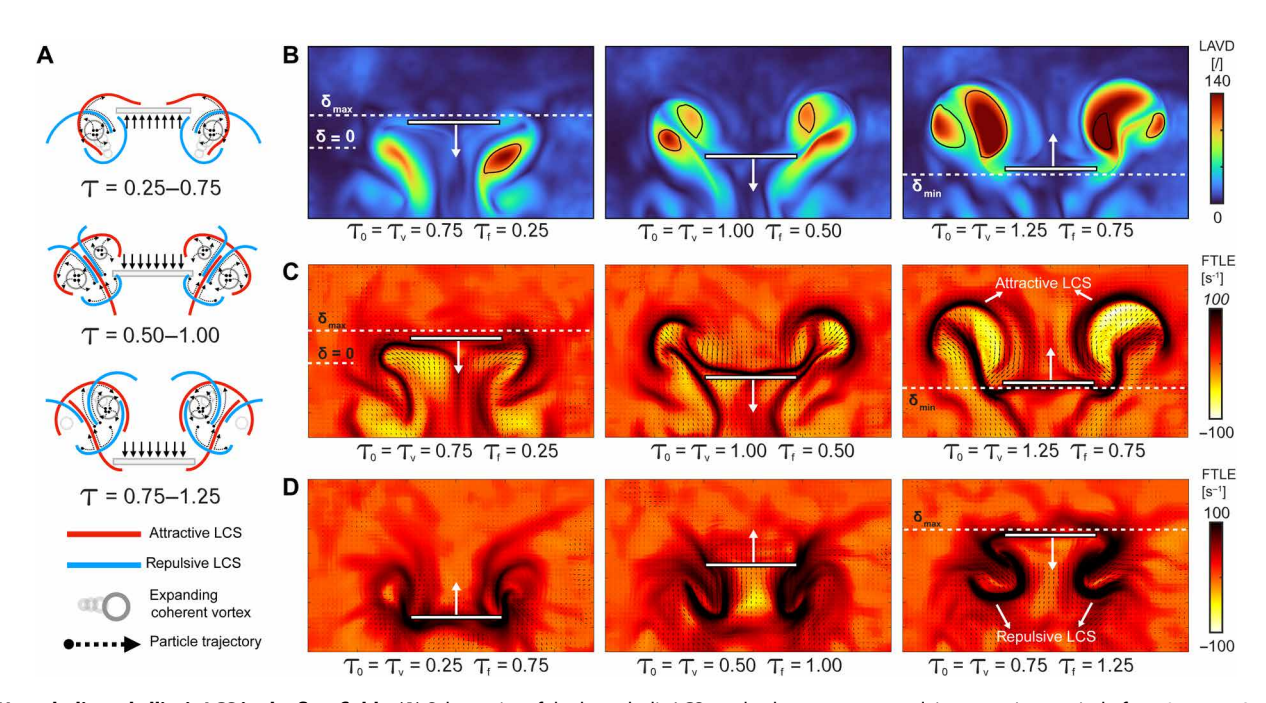


Fig. 3. Hyperbolic and elliptic LCS in the flow fields. (A) Schematics of the hyperbolic LCSs and coherent vortex evolving over time period of $\tau=0.75$ to 1.25. Particle trajectories are included in the evolution. (B) LAVD scalar fields (unitless) for the first full downstroke from max beam position in $+\hat{z}$ to min beam position in $-\hat{z}$, at $\tau=0.75$ to 1.25. δ_{max} and δ_{min} denote the maximum and minimum beam location, respectively, and δ_0 denotes the original beam position at t=0. (C) Backward finite-time Lyapunov exponent (b-FTLE) scalar fields for the same same time sequence. The attractive LCS are highlighted by high FTLE regions. Movie of the LAVD sequence is in movie S3; movie of the FTLE sequence is in movie S4. (D) Forward FTLE (f-FTLE) scalar fields for the same same time sequence. The repulsive hyperbolic LCS are highlighted by the high FTLE regions here. The integration period is $\tau=0.5$ here. For (B) to (D), the integration period is $\tau=0.5$; τ_0 is the starting frame of integration and also the frame of visualization τ_V for each figure, and τ_f is the final frame for integration.

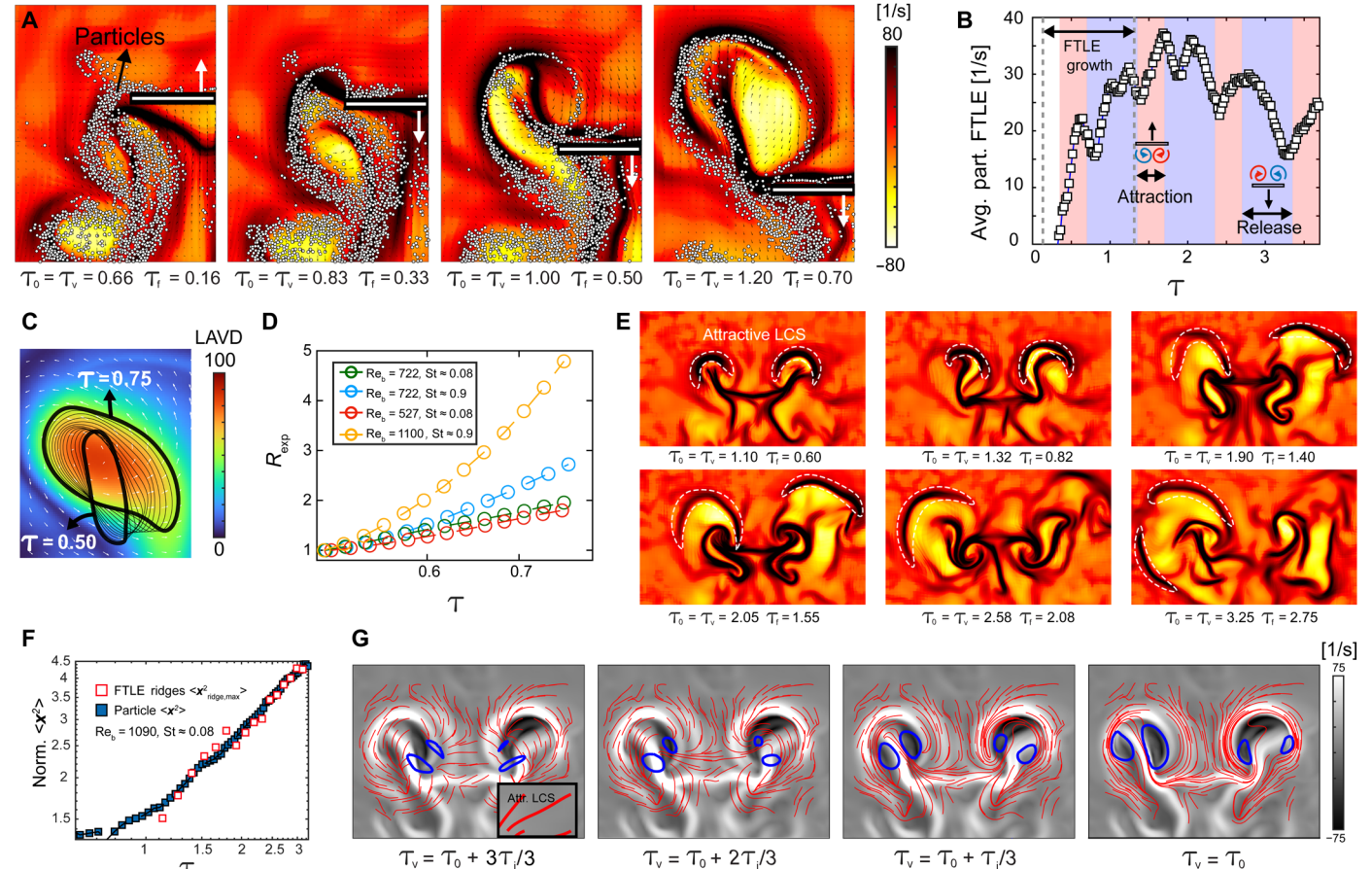


Fig. 4. Descriptions on LCS dynamics. (A) Experimental particle (pollen) tracking overlaid on FTLE fields for $\tau=0.66$ to 1.20, $[U_d,R_d]=[2.97~\text{ms}^{-1},1.60~\text{mm}]$. (B) Average backward FTLE at the particle locations for $\tau=0.00$ to 3.25, at the same drop condition. The LCS growth period from $\tau=0.00$ to 1.75 and the upstroke particle attraction, downstroke particle release periods are labeled. (C) Experimental time series of coherent vortex expansion for $\tau=0.50$ to 0.75; the background LAVD is obtained at $\tau=0.75$ (end of upstroke dispersion) and an integration period of $\tau=-0.25$. (D) Coherent vortex (RCV) expansion for $\tau\in[0.50~0.75]$ at different particle Stokes number and Reynolds number of vibration. (E) Advection of the attractive LCS at $\tau=1.10$ to 3.25. The integration periods are $\tau=-0.50$; the color bar is the same as in (A). For (A) and (E), τ_0 is the starting frame of integration and also the frame of visualization τ_v for each figure, and τ_f is the final frame for integration. (F) Normalized MSD for particles and maximum FTLE ridge locations. Both are normalized by the beam width b^2 . Same video source as in (E). (G) Step-by-step forward-time migration of attractive stretchlines (in red) onto high FTLE regions (background colormap), and the migration of coherent vortices (in blue lines) over $\tau\in[0.75~1.25]$ from $\tau_f=\tau_0+\tau_i=0.75$ to $\tau_0=1.25$. The FTLE integration period is $\tau_i=-0.50$ in backward time; thus, the migration in forward time starts at τ_f .

the attractive LCS. They primarily concentrate in the high FTLE ridges in Fig. 3C for the downstroke. Equivalently, regions with maximum repulsion, i.e., the repulsive LCS, are obtained with forward integration $\tau_i > 0$ as shown in high FTLE ridges of Fig. 3D, where particles are stretched apart the most in forward time (see full sequence in section S6 and movie S4). We will refer to these dark red regions with high FTLE values as FTLE ridges below, which typically coincide with LCS locations.

Combining with the coherent vortices, a more complete picture of spore dispersion from fluttering leaves can be depicted. Schematics in Fig. 3A illustrates these dynamics under the two types of LCS. From their generation at $\tau\approx 0.25$, upstroke vortices continue to eject particles outward, indicated also by the surrounding repulsive LCS in blue curves. As the downstroke vortex grows in strength, substantial shearing between the two sets of vortices develops, and their coupling creates attractive LCS that pulls particles outward as mentioned in Fig. 1. A cap-like attractive LCS then develops on the dipole exterior. It has multiple repulsive LCS penetrating by cooperatively pulling particles outward. The process completes as the substrate reaches

minimum position, and the nested hyperbolic LCS expands in size before weakening. During the downstroke, coherent vortices remain active in flux, ejecting more particles onto the nested structures.

Attractive flow profiles for particles are further validated by overlaying particle locations onto the FTLE map (backward integrated), shown in Fig. 4A. Extracting the FTLE values at these particle locations over time reveals the continuous growth of flow coherence up to the second cycle $\tau\approx 1.75$, as shown in Fig. 4B. FTLE increment indicates particles exiting high-vorticity regions and entering high-strain regions, resulting in particle entrapment on LCS. Cyclic rise and fall after $\tau\approx 1.75$ indicate that particles are pulled into attractive profiles during upstroke and released into the surrounding in a super-diffusive process during downstroke, confirming our finding in Fig. 2. Therefore, particle entrapment is only momentary, as the particles are released in each cycle.

The hyperbolic LCS can have prolonged influences on more distanced particles, since they can have a long lifetime, $\tau > 3$, as they expand and travel outward, demonstrated in Fig. 4E. The speed of advection is identical to that of the particle cluster boundary. This is

shown in Fig. 4F, where the normalized MSD measured at the particle ensemble front over time aligns well with the outermost FTLE ridge positions, $\kappa_{\text{ridge,max}}^2$. This is reasonable because the frontier of the flow stream discussed in Fig. 2 can possess an expanding, attractive LCS that pulls materials outward.

Backward FTLE ridges for the wheat leaf samples are also extracted and shown in section S6. Similar attractive LCS profiles to Fig. 3B are displayed, validating the surrogate beam model.

Flow dynamics from geodesic transport theory

While FTLE diagnostics render the approximate locations of the LCS, ridges are merely coherence imprints that are left behind by true LCS in the flow. For a more rigorous identification, we turned to the geodesic transport theory (37) to calculate the attractive LCS as material lines (a set of fluid elements) in the 2D domain. For each fluid patch that is shown in the domain of Fig. 3 (B to D), an attractive LCS (red line) can be calculated over $t \in [t_0, t_0 + \tau_i T]$ as shown in the inset of Fig. 4G. In forward time, these LCS first attract particles in the fluid patch and then pull the whole fluid patch forward with itself as the center backbone. Eventually, at the end of integration, many of them land near the FTLE ridges, an imprint left by this migration dynamics. The dynamics sequence is shown for the downstroke in Fig. 4G with backward FTLE map and coherent vortices overlaid. Similar analysis is documented in literature for geophysical flows (38).

The particle landing proximity to FTLE ridges depends on the Stokes number. Particles with St ≈ 1 exhibit more preferential concentration and pattern formation near the FTLE ridges, as the inertia of particles introduces bias in trajectories toward low-vorticity, high-strain regions, commonly observed in literature (39, 40). This effect at unity suggests aggregation as a result of particle relaxation occurring on the same time scale as the flow. Increasing St above one, particles start to decouple from the flow due to gravity and inertia, losing preferential patterning again. St, $r_{\rm p}$, and $\rho_{\rm p}$ of common bioaerosols and experimented particles used are reported in Table 1.

DISCUSSION

To further analyze the vortex energy budget, we approximated the kinetic energy of the vortices as $E_{\Gamma} \sim \rho_{\rm a} \Gamma^2 L_{\Gamma} (41)$, where L_{Γ} is the length of the connected vortex tube. This allowed us to compare the energy budget spent in vortex generation via drop impact on stationary versus flexible surfaces. We first estimated $\Gamma_{\rm stat.} \approx 0.1 U_{\rm d} R_{\rm d} {\rm Re_{\rm d}^{3/8} Re_{\rm e}^{-1/4}}$, where

Re_a = $U_{\rm d}(2R_{\rm d})/\nu_{\rm a}$ from (32) and obtained $\Gamma_{\rm flex}$. from the above analysis. With varying input drop energy $E_{\rm d}=0$ to 50 mJ from a natural range of $[U_{\rm d},R_{\rm d}]$, we calculated the ratio of the rotational energy to the drop kinetic energy, $E_{\rm F}/E_{\rm d}$. For a flexible leaf surface, $E_{\rm F}/E_{\rm d}=2.5$ to 5.5%, whereas $E_{\rm F}/E_{\rm d}=0.5$ to 1.5% for a stationary leaf across the parameter space. Leaf elasticity allows for a more substantial allocation of energy to vortex generation, a key role that has been largely omitted in leaf-spore dispersion mechanics.

In summary, we have developed a comprehensive model that characterizes how pathogenic spores escape vibrating leaves via a flow stream enabled by leaf elasticity. The local acceleration of the vibrating substrate here dominates over the background advection (i.e., Strouhal number, $Str = fA / U_{bkg.} \gg 1$), which allows us to parametrically analyze the drop-leaf mechanics alone. We showed a linear coupling between impinging drop inertia, leaf vibration speed, and flux strength from leaf edges, summarized nondimensionally as $Re_b \propto C_M Re_d$ and $Re_{st} \approx 0.12 Re_b$. From linear approximation, we obtained empirically that the overall particle dispersion speed scales with vibration as $Re_{disp.} \approx 0.5 Re_b$ for $Re_b < 1800$. We proved that, even in the absence of ambient eddies, raindrop impacts alone can power a dispersion stream for surface-bound pathogens such as fungal spores. Using LCS diagnostics, we further revealed the airborne spore transport pathways. Using physical modeling through dynamical system's approach, we proposed here a physical explanation for the co-occurrence of rainfall and bio-aerosol dispersion in the atmosphere (8).

Therefore, the current study advances our current understanding of spore dispersal avenues (14, 42–45) and brings together impact mechanics and Lagrangian coherence to uncover an omitted spore dispersion mechanism that is less reliant on passive environmental carriers such as traveling splashed droplets or background canopy currents. The synergistic coupling of leaf elasticity and rainfall perturbation is established here and the hitherto-hidden lateral escape routes for pathogenic aerosols dwelling on leaf surfaces are visualized. Potential improvements to the model, such as incorporating leaf shape variations or spatial coupling between neighboring plant structures could lead to more customized crop infection controls in the future.

METHODS

Drop-impact experiments

High-speed photography (FASTCAM, Photron) at 1000 to 3000 fps is used. A flapping wheat leaf is mechanically modeled as an angularly

| Particle types | $ ho_{ m p}$ (g/cm 3) | r _p (μm) | St |
|---|---------------------------|---------------------|---|
| Soda lime glass sphere (SGS)* | 2.5 | 10 | 0.020-0.080 |
| Glycerine-water smoke* | 1.0 | 1.0–2.0 | $1.0 \times 10^{-4} - 4.0 \times 10^{-3}$ |
| Pine (Pinus contorta) pollen* | 1.2 (<i>47</i>) | 20–25 | 0.10-0.90 |
| Forget-Me-Not (<i>Mimetes palustris</i>) pollen | 1.2 (47) | 2.5–5.0 (48) | $2.0 \times 10^{-3} - 5.0 \times 10^{-3}$ |
| Wheat rust (<i>Puccinia triticina</i>) spore | 1.0 (44) | 10 (<i>14</i>) | 0.020-0.10 |

flapping thin cantilever beam; thin polycarbonate beams, $\rho_b = 1220 \text{ kg/m}^3$, are used exprimentally, whose dimensions, rigidity, and wetting conditions are documented in section S1, along with that of the wheat samples. Mechanically, the beam substrate is fixed by clamping on one end along the longitudinal axis. The rotational degree of freedom around the longitudinal axis is thus limited with the high L/b ratio used and the center impact along this axis. After securing the beam, drop impacts are induced with a syringe pump at a pumping rate of 0.2 mm/min. An impact is induced 10 mm away from the tip of the beam to observe the maximum impact consequences. The location is chosen to prevent substantial spillage as well, since the maximum spreading radius $R_{\rm m}$ can be calculated as 6 to 11 mm, with $R_{\rm m} \approx (1/2)R_{\rm d}Re_{\rm d}^{1/4}$ from the aforementioned $[U_{\rm d}, R_{\rm d}]$ conditions (14). Combinations of beam, drop, and impact velocity tested in Fig. 2G are listed in section S4.

Visualization methodology

Particle visualization uses the use of glass particles and pine pollens. They are uniformly deposited on top of the substrate surfaces prior to the drop impact experiment, with size, density, and Stokes number, St = $t_{\rm p}/t_{\rm f}$, reported in Table 1. Particle layer thickness is consistent with experimentation methodology in (14), at 0.1 to 0.2 mm. Particle size and density ranges are typically $r_{\rm p}=1.0$ to 20.0 μ m and $\rho_{\rm p}=1.0$ to 2.5 \times 10³ kg/m³ respectively.

Smoke visualization is used to perform 2D DPIV on the 2D transverse cross section, in order to extract the velocity and vorticity fields at the location of impact and shedding. Chauvet smoke machine is paired with a 40:60 glycerol-water mixture to produce a thick smoke layer that fills the field of view. A laser beam (sheet laser) with the intensity of 5 mW is used to illuminate the smoke layer at the 2D transverse cross section of impact point, with laser sheet thickness of 0.2 to 0.5 mm. DPIV is conducted with the MATLAB package PIVLab by Thielicke (46). CLAHE is enabled with window size 64 as the only image setting. The analysis uses an FFT window deformation with three passes; pass 1 is integration area of 120 pixel and 64-pixel step; pass 2 is integration area of 64 pixel and 32-pixel step; pass 3 is integration area of 32 pixel and 16-pixel step. Gauss 2X3-point estimator is used with high correlation robustness. The error of the velocity vectors in most domain regions are estimated to be 0.0128 m/s from difference of actual tracer measurements and DPIV analysis, an error rate of 2 to 10%. High-velocity vortex centers typically have larger velocity vector errors from observation. From PIV correlation coefficients map of the velocity fields, we observed that correlation coefficients are at 0.9 to 1.0 for most of the domain, except at the corners/ edges of the domain and the center regions of vortices, which are observed to have spots with coefficients as low as 0.4 to 0.6. This can potentially yield errors and 2D divergence in measurements. Please see section S2 for more discussion on divergence quantification on the *yz* domain.

To extract iLCS in air which needs the particle velocity fields $\mathbf{u}_{\mathbf{p}}(x,\,t)$, we use a methodology different from simple particle and smoke visualizations. Because of the difficulty to directly seed air with inertial particles ($\rho_a\ll\rho_p$), we use smoke particle tracers as initial background seeding. Then, we initiate drop impacts onto the beam/leaf structure with particles and let particles aboard the beam to spread into the surrounding air space in generated flows, thereby obtaining velocity fields $\mathbf{u}_{\mathbf{p}}(x,\,t)$ for the entire domain. The smoke fills in such early "empty" regions outside, which has trivial impacts to flow generation. Nonetheless, this introduces systematic errors in

particle "empty" regions with only smoke seeding, since they will carry minimal inertial signatures. To further justify the necessity of this method and quantify the errors, we have added additional discussions in section S6.

All the conclusions are drawn from the above visualization experiments and data. For particle dispersal experiments, 3 to 15 samples per condition are tested. PIV data and vorticity measurements have an average sample size per condition of two to four. LAVD and FTLE map measurements are unique for each experimental trial, thus not subjected to statistical averaging. Expansion ratio data has an average sample size of three to five.

Supplementary Materials

This PDF file includes:

Sections S1 to S6 Figs. S1 to S16 Legends for movies S1 to S4 References

Other Supplementary Material for this manuscript includes the following: Movies S1 to S4

REFERENCES AND NOTES

- R. N. Strange, P. R. Scott, Plant disease: A threat to global food security. Annu. Rev. Phytopathol. 43, 83–116 (2005).
- J. B. Ristaino, P. K. Anderson, D. P. Bebber, K. A. Brauman, N. J. Cunniffe, N. V. Fedoroff, C. Finegold, K. A. Garrett, C. A. Gilligan, C. M. Jones, M. D. Martin, G. K. M. Donald, P. Neenan, A. Records, D. G. Schmale, L. Tateosian, Q. Wei, The persistent threat of emerging plant disease pandemics to global food security. *Proc. Natl. Acad. Sci. U.S.A.* 118, e2022239118 (2021).
- P. Skamnioti, S. J. Gurr, Against the grain: Safeguarding rice from rice blast disease. Trends Biotechnol. 27, 141–150 (2009).
- P. K. Anderson, A. A. Cunningham, N. G. Patel, F. J. Morales, P. R. Epstein, P. Daszak, Emerging infectious diseases of plants: Pathogen pollution, climate change and agrotechnology drivers. *Trends Ecol. Evol.* 19, 535–544 (2004).
- J. K. M. Brown, M. S. Hovmøller, Aerial dispersal of pathogens on the global and continental scales and its impact on plant disease. Science 297, 537–541 (2002).
- D. G. Schmale III, S. D. Ross, Highways in the sky: Scales of atmospheric transport of plant pathogens. *Annu. Rev. Phytopathol.* 53, 591–611 (2015).
- J. M. Hirst, O. J. Stedman, Dry liberation of fungus spores by raindrops. *Microbiology* 33, 335–344 (1963).
- J. A. Huffman, A. J. Prenni, P. J. DeMott, C. Pöhlker, R. H. Mason, N. H. Robinson, J. Fröhlich-Nowoisky, Y. Tobo, V. R. Després, E. Garcia, D. J. Gochis, E. Harris, I. Müller-Germann, C. Ruzene, B. Schmer, B. Sinha, D. A. Day, M. O. Andreae, J. L. Jimenez, M. Gallagher, S. M. Kreidenweis, A. K. Bertram, U. Pöschl, High concentrations of biological aerosol particles and ice nuclei during and after rain. Atmos. Chem. Phys. 13, 6151–6164 (2013).
- J. M. Cevallos-Cevallos, G. Gu, M. D. Danyluk, N. S. Dufault, A. H. C. van Bruggen, Salmonella can reach tomato fruits on plants exposed to aerosols formed by rain. *Int. J. Food Microbiol.* 158, 140–146 (2012).
- P. A. Hobson, P. C. H. Miller, P. J. Walklate, C. R. Tuck, N. M. Western, Spray drift from hydraulic spray nozzles: The use of a computer simulation model to examine factors influencing drift. J. Agric. Eng. Res. 54, 293–305 (1993).
- S. Basu, A. Yawar, A. Concha, M. M. Bandi, On angled bounce-off impact of a drop impinging on a flowing soap film. Fluid Dyn. Res. 49, 065509 (2017).
- J. M. Cevallos-Cevallos, M. D. Danyluk, G. Gu, G. E. Vallad, A. H. C. van Bruggen, Dispersal of salmonella typhimurium by rain splash onto tomato plants. *J. Food Prot.* 75, 472–479 (2012).
- M. Mircea, S. Stefan, S. Fuzzi, Precipitation scavenging coefficient: Influence of measured aerosol and raindrop size distributions. Atmos. Environ. 34, 5169–5174 (2000).
- S. Kim, H. Park, H. A. Gruszewski, D. G. Schmale III, S. Jung, Vortex-induced dispersal of a plant pathogen by raindrop impact. *Proc. Natl. Acad. Sci. U.S.A.* 116, 4917–4922 (2019).
- D. L. Whitaker, J. Edwards, Sphagnum moss disperses spores with vortex rings. Science 329, 406 (2010).
- J. Edwards, D. Whitaker, S. Klionsky, M. J. Laskowski, A record-breaking pollen catapult. Nature 435, 164–164 (2005).

SCIENCE ADVANCES | RESEARCH ARTICLE

- J. Zhang, S. Childress, A. Libchaber, M. Shelley, Flexible filaments in a flowing soap film as a model for one-dimensional flags in a two-dimensional wind. *Nature* 408, 835–839 (2000).
- S. Gart, J. E. Mates, C. M. Megaridis, S. Jung, Droplet impacting a cantilever: A leaf-raindrop system. *Phys. Rev. Appl.* 3, 044019 (2015).
- P. Orkweha, A. Downing, A. P. Lebanoff, S. Zehtabian, S. S. Bacanli, D. Turgut,
 A. K. Dickerson, Ensemble machine learning predicts displacement of cantilevered fibers impacted by falling drops. *J. Fluids Struct.* 102, 103253 (2021).
- S. Alben, M. Shelley, Coherent locomotion as an attracting state for a free flapping body. Proc. Natl. Acad. Sci. U.S.A. 102, 11163–11166 (2005).
- S. Alben, C. Witt, T. V. Baker, E. Anderson, G. V. Lauder, Dynamics of freely swimming flexible foils. *Phys. Fluids* 24, 051901 (2012).
- K. J. Niklas, A mechanical perspective on foliage leaf form and function. New Phytol. 143, 19–31 (1999).
- 23. G. Haller, Lagrangian coherent structures. Annu. Rev. Fluid Mech. 47, 137–162 (2015).
- M. Serra, P. Sathe, I. Rypina, A. Kirincich, S. D. Ross, P. Lermusiaux, A. Allen, T. Peacock, G. Haller, Search and rescue at sea aided by hidden flow structures. Nat. Commun. 11, 2225 (2020)
- S. C. Shadden, J. O. Dabiri, J. E. Marsden, Lagrangian analysis of fluid transport in empirical vortex ring flows. *Phys. Fluids* 18, 047105 (2006).
- H. Park, S. Kim, H. A. Gruszewski, D. G. Schmale III, J. B. Boreyko, S. Jung, Dynamics of splashed droplets impacting wheat leaves treated with a fungicide. J. R. Soc. Interface. 17, 20200337 (2020).
- S. Kim, Z. Wu, E. Esmaili, J. J. Dombroskie, S. Jung, How a raindrop gets shattered on biological surfaces. Proc. Natl. Acad. Sci. U.S.A. 117, 13901–13907 (2020).
- J. O. Laws, D. A Parsons, The relation of raindrop-size to intensity. Eos Trans. AGU 24, 452–460 (1943)
- E. Villermaux, B. Bossa, Single-drop fragmentation determines size distribution of raindrops. Nat. Phys. 5, 697–702 (2009).
- W. R. Jarvis, The dispersal of spores of botrytis cinerea fr. in a raspberry plantation. *Trans. Brit. Mycol. Society* 45, 549–559 (1962).
- J. Lee, Y.-J. Park, U. Jeong, K.-J. Cho, H.-Y. Kim, Wake and thrust of an angularly reciprocating plate. J. Fluid Mech. 720, 545–557 (2013).
- S. Alben, M. J. Shelley, Flapping states of a flag in an inviscid fluid: Bistability and the transition to chaos. *Phys. Rev. Lett.* 100, 074301 (2008).
- C. H. K. Williamson, A. Roshko, Vortex formation in the wake of an oscillating cylinder. J Fluids Struct. 2, 355–381 (1988).
- N. D. Ebrahimi, J. D. Eldredge, Y. S. Ju, Wake vortex regimes of a pitching cantilever plate in quiescent air and their correlation with mean flow generation. *J Fluids Struct.* 84, 408–420 (2019).
- G. Haller, A. Hadjighasem, M. Farazmand, F. Huhn, Defining coherent vortices objectively from the vorticity. J. Fluid Mech. 795, 136–173 (2016).
- A. Provenzale, Transport by coherent barotropic vortices. Annu. Rev. Fluid Mech. 31, 55–93 (1999).
- G. Haller, F. J. Beron-Vera, Geodesic theory of transport barriers in two-dimensional flows. Phys. D. Nonlinear Phenom. 241, 1680–1702 (2012).
- 38. F. J. Beron Vera, Flow coherence: Distinguishing cause from effect (Springer, 2015) pp. 81–89.
- S. Goto, J. C. Vassilicos, Sweep-stick mechanism of heavy particle clustering in fluid turbulence. *Phys. Rev. Lett.* **100**, 054503 (2008).
- T. Sapsis, G. Haller, Clustering criterion for inertial particles in two-dimensional time-periodic and three-dimensional steady flows. Chaos 20, 017515 (2010).
- 41. H. Kim, J. Lee, T.-H. Kim, H.-Y. Kim, Spontaneous marangoni mixing of miscible liquids at a liquid–liquid–air contact line. *Langmuir* **31**, 8726–8731 (2015).
- E. Dressaire, L. Yamada, B. Song, M. Roper, Mushrooms use convectively created airflows to disperse their spores. Proc. Natl. Acad. Sci. U.S.A. 113, 2833–2838 (2016).

- 43. P. H. Gregory, The operation of the puff-ball mechanism of lycoperdon perlatum by raindrops shown by ultra-high-speed schlieren cinematography. *Trans. Brit. Mycol. Society* 32, 11–15 (1049)
- M. Roper, A. Seminara, M. M. Bandi, A. Cobb, H. R. Dillard, A. Pringle, Dispersal of fungal spores on a cooperatively generated wind. *Proc. Natl. Acad. Sci. U.S.A.* 107, 17474–17479 (2010).
- 45. C.T. Ingold, Fungal spores: Their libération and dispersal (Clarendon Press, ed. 4, 1971).
- W. Thielicke, E. Stamhuis, Pivlab-towards user-friendly, affordable and accurate digital particle image velocimetry in matlab. J. Open Res. Softw. 2, 25 (2014).
- L. M. Sosnoskie, T. M. Webster, D. Dales, G. C. Rains, T. L. Grey, A. S. Culpepper, Pollen grain size, density, and settling velocity for palmer amaranth (amaranthus palmeri). Weed Science 57, 404–409 (2009).
- 48. C. A. Knight, R. B. Clancy, L. Götzenberger, L. Dann, J. M. Beaulieu, On the relationship between pollen size and genome size. *J. Bot.* **2010**, 1–7 (2010).
- M. Pasandideh-Fard, Y. M. Qiao, S. Chandra, J. Mostaghimi, Capillary effects during droplet impact on a solid surface. *Phys. Fluids* 8, 650–659 (1996).
- M. Long, J. Hasanyan, S. Jung, Spreading dynamics of a droplet impacting a sphere. Phys. Fluids 34, 102115 (2022).
- S. Jung, Swimming, flying, and diving behaviors from a unified 2D potential model. Sci. Rep. 11, 15984 (2021).
- 52. T. Y. Wu, Fish swimming and bird/insect flight. Annu. Rev. Fluid Mech. 43, 25–58 (2011).
- M. R. Maxey, J. J. Riley, Equation of motion for a small rigid sphere in a nonuniform flow. Phys. Fluids 26, 883–889 (1983).
- G. Haller, F. J. Beron-Vera, Coherent lagrangian vortices: The black holes of turbulence. J. Fluid Mech. 731, R4 (2013).
- G. Haller, T. Sapsis, Where do inertial particles go in fluid flows? Phys. D. Nonlinear Phenom.
 237. 573–583 (2008).
- F. J. Beron-Vera, Nonlinear dynamics of inertial particles in the ocean: From drifters and floats to marine debris and Sargassum. Nonlinear Dyn. 103, 1–26 (2021).
- G. Haller, G. Yuan, Lagrangian coherent structures and mixing in two-dimensional turbulence. *Phys. D. Nonlinear Phenom.* 147, 352–370 (2000).
- M. Farazmand, D. Blazevski, G. Haller, Shearless transport barriers in unsteady two-dimensional flows and maps. Phys. D. Nonlinear Phenom. 278-279, 44–57 (2014).
- F. J. Beron-Vera, M. J. Olascoaga, G. Haller, M. Farazmand, J. Triñanes, Y. Wang, Dissipative inertial transport patterns near coherent Lagrangian eddies in the ocean. *Chaos* 25, 087412 (2015).

Acknowledgments: Wheat samples are grown at the Plant Breeding and Genetics Section, School of Integrative Plant Breeding and Genetics Section at Cornell University. Please see wheat preparation details in the section S1. Funding: This work was supported by the National Science Foundation grant no. ISO-2120739. The collaboration between F.J.B.-V. and S.J. was initiated at the Aspen Center for Physics, which is supported by the National Science Foundation grant no. PHY-1607611. Author contributions: S.J. and S.K. conceived the project. Z.W. designed and carried out the experiments, conducted analysis and wrote the paper. S.B. contributed to the discussion and critique on vortex shedding. M.S. prepared and provided wheat samples. F.J.B.-V. provided the elliptic and hyperbolic LCS calculation tools and relevant discussions. All authors discussed and edited the manuscript. Competing interests: The authors declare that they have no conflicts of interest. Data and availability: All data needed to evaluate the conclusions are present in the paper and/or the Supplementary Materials. The data used in this study are also deposited in the public repository at this location: https://osf. io/dkmwi/.

Submitted 18 July 2023 Accepted 2 January 2024 Published 31 January 2024 10.1126/sciady.adi8092